

A Plasma Torus Around a Young Low-Mass Star

Luke G. Bouma^{1,2}

¹*Observatories of the Carnegie Institution for Science, Pasadena, CA 91101, USA*

²*Carnegie Fellow*

Roughly one percent of red dwarfs younger than 100 million years show structured, periodic optical light curves suggestive of transiting opaque material that corotates with the star^{1–4}. The composition, origin, and even the existence of this material are uncertain. The main alternative hypothesis is that these complex periodic variables (CPVs) are explained by complex distributions of bright or dark regions on the stellar surfaces⁵. Here, we present time-series spectroscopy and photometry of a rapidly-rotating ($P=3.9$ hr) CPV, TIC 141146667. The spectra show coherent sinusoidal Balmer emission at twice to four times the star’s equatorial velocity, demonstrating the existence of extended clumps of circumstellar plasma — a plasma torus. Given that long-lived condensations of cool (10^4 K) plasma can persist in the hot (10^6 K) coronae of stars with a wide range of masses^{6–11}, these data support the idea that around the lowest-mass stars, such condensations can be optically thick; the exact origin of the material and its microphysical opacity remain unclear.

1 Main

M dwarfs, stars with masses below about half that of the Sun, are the only type of star to offer near-term prospects for detecting the atmospheres of rocky exoplanets with surface water¹². Investment with JWST has proceeded accordingly. How an M dwarf’s evolution influences its planets—especially the retention of their atmospheres—has concurrently become a major theme in exoplanet and stellar astrophysics. Previous work has established that most M dwarfs host close-in planets¹³ that are often subject to long circumstellar disk lifetimes¹⁴, to large doses of UV radiation¹⁵, and to a high incidence of flares and coronal mass ejections¹⁶. Nevertheless, despite excellent work in these areas, the properties of the plasma and magnetospheric environments that bathe the young, close-in exoplanets have remained challenging to quantify.

One glaring example of our current ignorance is the complex periodic variables (CPVs). While Figure 1 highlights the main object of interest in this article, over one hundred analogous objects have now been found by K2 and TESS^{1–4,17,18}. These CPVs are phenomenologically identified based on their highly structured and periodic optical light curves; most are M dwarfs with rotation periods shorter than two days. Within current sensitivity limits, none have primordial disks^{2,4}. However, $\approx 3\%$ of stars a few million years old show this behavior, and the observed fraction decreases to $\approx 0.3\%$ by ≈ 150 Myr¹⁸.

The two leading hypotheses to explain the CPVs are either that transiting clumps of circumstellar material corotate with the star^{2,4,19}, or that these stars represent an extreme in naturally-

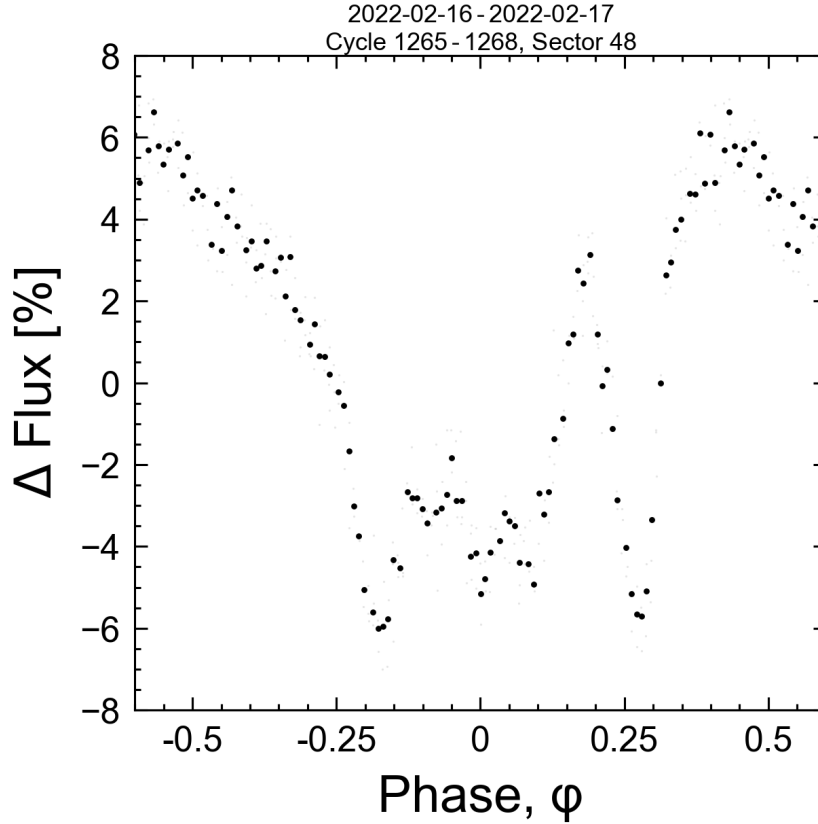


Figure 1: **Figure 1 (Movie): TIC 141146667 is a complex periodic variable (CPV).** For the best experience, please view the online movie available [here](#), which spans a baseline of 5,784 cycles irregularly sampled over three years. The TESS light curve is phased to the 3.930 hour period in groups of a few cycles per frame. This is the period both of stellar rotation, and (we hypothesize) of corotating clumps of circumstellar material. Raw data acquired with two minute sampling are in gray; black is their average. Similar to other members of this class, the sharp photometric features persist for tens to thousands of rotational cycles.

occurring distributions of starspots or faculae⁵. Currently, the main argument against a starspot-only explanation invokes the timescales and amplitudes of the sharpest photometric features. However, no independent evidence has yet been acquired for the presence of any circumstellar material. Geometrically, transiting clumps would imply an occurrence a few to at most ten times the observed rate. Such clumps could therefore exist around 10-30% of M dwarfs during their early lives.

The dearth of evidence for circumstellar material around CPVs is surprising given that separate studies of young stars have, for decades, reported that stellar coronae contain both hot (10^6 K) and cool (10^4 K) plasma. In particular, time-series spectroscopy for stars with a wide range

of masses has shown periodic high-velocity absorption and emission in Balmer lines such as $H\alpha$, interpreted as long-lived, corotating clumps of cool plasma^{6,8,20,21}. Such clumps are forced into corotation by the magnetic field, and the exact geometry of where the plasma can accumulate is dictated by the field’s topology. For instance, a tilted dipole field tends to yield an accumulation surface of a warped torus⁷, whereas in the limit of a single strong field line, accumulation occurs at the line’s apex, furthest from the star¹⁰. To date, none of these spectroscopic variables have shown any photometric anomalies⁴, leaving open the issue of whether they are related to CPVs.

In this study, we present the first observations of corotating clumps of cool plasma around a CPV. We identified TIC 141146667 in previous work⁴ by searching the TESS two-minute data²² for stars showing at least three sharp and periodic dips per cycle. We selected the star for spectroscopy because its brightness and rapid rotation offer sensitivity to small variations in the line profiles. We observed for five hours on 17 February 2024 (UT) using the High Resolution Echelle Spectrometer (HIRES;²³) on the Keck I 10m telescope. TESS observed the star over a four week period from 30 January 2024 to 26 February 2024 with a duty cycle of 77%. During the spectral observations, TESS was performing a data downlink; TESS data collection resumed 12 hours (three rotation cycles) after the spectra were acquired. Extended Data Figure 1 shows the detailed photometric behavior of the star before and after the exact epoch of observation; the photometric morphology is similar before and after the data gap.

2 Results

Figure 2 shows the data from February 2024. Over timescales of years, CPVs maintain the same period, while their photometric morphology evolves. TIC 141146667 indeed evolved relative to the February 2022 discovery data⁴. In the February 2024 data, the average photometric signal showed a small brightening over 45% of the period, followed by a complex flux dip spanning 55% of the period. This eclipse feature shows two to three local photometric minima, and one to two local maxima. Its W-shape is suggestive of eclipse geometries seen in some forward models of warped plasma tori²⁴.

The spectroscopy shows emission well beyond the star’s equatorial velocity ($v_{\text{eq}}=130 \text{ km s}^{-1}$). There are at least two distinct emission components, separated by half a cycle in phase. The first component has clearer sinusoidal behaviour and is double-peaked, with peak semi-amplitudes of $K_1=2.1 v_{\text{eq}}$ and $2.7 v_{\text{eq}}$. There is significant non-periodic variability in this double-peaked component: the flux excess from both peaks begins with an amplitude equal to 100% of the continuum flux early in the observation sequence, and falls to 30% by its end. The component 180° opposite in phase is similarly only detected from $\phi=0.2$ -1.0. From $\phi=0.2$ -0.5, this latter component appears connected to the star in velocity space. While its peak semi-amplitude of $K_1=3.9 v_{\text{eq}}$ is achieved at both $\phi=0.25$ and 0.75 , its amplitude decreases from a 60% excess over the continuum at the beginning of the observation sequence to a 10% excess by its end. The sinusoidal period for all of these emission components is consistent with the photometric 3.930 hour period.

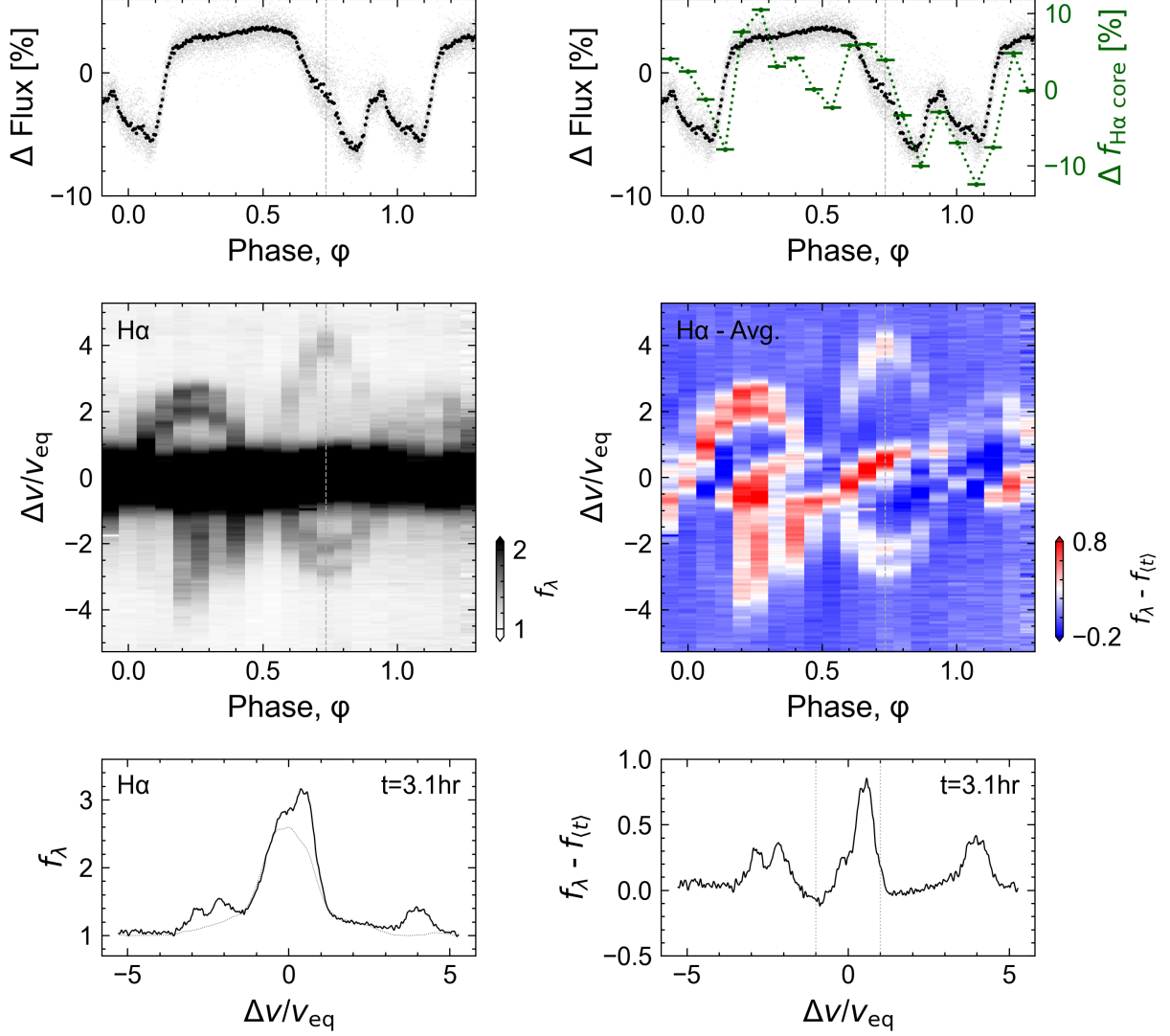


Figure 2: **Figure 2 (Movie):** Hydrogen emission from circumstellar plasma orbiting TIC 141146667. (TODO)For the best experience, please view the online movie available here. **Panel a:** TESS light curve from UT 2024-02-05 to UT 2024-02-26 folded on the 3.930 hour period. Black points are averaged; gray are the raw data. **Panel b:** Keck/HIRES H α spectra acquired on UT 2024-02-17. The continuum is set to unity, and the darkest color is set at twice the continuum to accentuate emission outside the line core ($|v/v_{\text{eq}}| > 1$, for $v_{\text{eq}}=130\text{ km s}^{-1}$). While emission in the line core originates in the stellar chromosphere, the sinusoidal emission features are most readily described by a warped plasma torus. **Panel c:** Individual epochs of Panel b, visible in the online movie. The dotted line shows a time-averaged spectrum, $f_{(t)}$. **Panel d:** As in Panel a, but overplotting the median-normalized H α light curve at $|v/v_{\text{eq}}| < 1$. **Panel e:** As in Panel b, after subtracting the time-averaged spectrum. In addition to circumstellar emission, the line core shows absorption during the plasma clump transits. The asymmetric stretch is set to match the dynamic range of the data. **Panel f:** Individual epochs of Panel e, visible in the online movie.

These sinusoidal emission features require circumstellar clumps of partially-ionized hydrogen to be corotating with the star. Based on its period, this material’s motion is not Keplerian; it can only be explained by plasma being dragged along with the rotating stellar magnetic field. The velocity semi-amplitude of the sinusoids then gives the distance of the clumps from the stellar surface: $2.1\text{--}2.7 R_\star$ for the closer clump, and $3.9 R_\star$ for the other. These clumps transit in front of the star when passing from negative to positive velocity. This implies that the spectroscopic transit of the $2.1\text{--}2.7 R_\star$ clump occurs simultaneously with the sharp photometric spike visible in the TESS data.

The behavior within the stellar $H\alpha$ line core, at $|\Delta v/v_{\text{eq}}| < 1$, is more complex than outside it. For stars of this age and spectral type, one would expect emission in the line core to be generated in the stellar chromosphere and then modulated by any occulting material capable of absorbing or emitting $H\alpha$ photons. In Figure 2e, the behavior from $\phi=0.4\text{--}1.2$ has a simple interpretation: from $\phi=0.4\text{--}0.9$, a hot region first gradually crosses the stellar line profile, followed from $\phi=0.7\text{--}1.2$ by the transit of a cool region. Phases $\phi < 0.4$ show a mix of similar events, though the time sampling is sufficiently coarse that the interpretation is less clear. A final exercise to quantify the behavior in the line core is shown in Figure 2d, where $f_{H\alpha \text{ core}}$ denotes the summed flux at $|\Delta v/v_{\text{eq}}| < 1$. This panel shows that changes in the line core flux are usually correlated with the broadband variability, except at $\phi=0.5$, during the transit of the $3.9 R_\star$ clump and the occultation of the lower-velocity clump.

3 Discussion

Spectra of magnetically-active, rapidly rotating stars with a wide range of masses have been known to exhibit both sinusoidal emission features^{7,8,20,21} as well as transient absorption features in their line cores^{6,27,28} similar to Figure 2. No such stars were previously known to show complex light curves⁴. The usual interpretation for such spectroscopic variability comes from an analogy to quiescent solar prominences, which are cool condensations of plasma in the solar corona that can last days to weeks²⁹. In our Sun’s magnetosphere, these condensations fall back to the solar surface because gravity is stronger than any magnetic or centrifugal force capable of sustaining them. However for stars with magnetospheric radii R_m that exceed their corotation radii R_c , the effective potential experienced by a charged particle can have a local minimum outside R_c , enabling the material to be sustained for much longer timescales^{9,11}. Generally speaking, such material need neither transit, nor be optically thick.

Our Keck/HIRES observations are the first reported time-series spectra of a CPV, and they show that corotating circumstellar plasma clumps are present in at least one such star. Characteristic densities and masses of these clumps are $n \sim 10^{10} \text{ cm}^{-3}$ and $M \sim 10^{14} \text{ kg}$ (see Supplementary Methods Section 3), a similar density to solar prominences, but ten to one hundred times more massive. This observation rules out a “starspot-only” origin scenario for CPVs,⁵ since such scenarios have no means of explaining spectroscopic emission beyond the stellar disk. Similarly, scenarios

Table 1: Selected System Parameters for TIC 141146667

Parameter	Description	Value	Source
T_{eff}	Effective Temperature (K)	2972 ± 40	1
R_*	Stellar radius (R_\odot)	0.42 ± 0.02	1
Age	Stellar age range (Myr)	35-150	2
M_*	Stellar mass (M_\odot)	0.22 ± 0.02	3
γ	Systemic radial velocity (km s^{-1})	0.61 ± 1.47	4
Spec. Type	Spectral Type	M5.5Ve	4
P_{rot}	Rotation period (hr)	3.930 ± 0.001	5
v_{eq}	Equatorial velocity	130 ± 4	6
	($2\pi R_*/P_{\text{rot}}$) (km s^{-1})		
$v_{\text{eq}} \sin i_*$	Projected rotational	138 ± 8	4
	velocity (km s^{-1})		
i_*	Stellar inclination	> 63	4
	2σ lower limit (deg)		
d	Distance (pc)	57.54 ± 0.09	7
R_c	Keplerian corotation	1.82 ± 0.10	6
	radius (R_*)		
a_1	Clump 1 orbital radius (R_*) ...	2.1-2.7	4
a_2	Clump 2 orbital radius (R_*) ...	3.9	4
$\langle \text{EW}_{\text{H}\alpha} \rangle$	Time-averaged H α line core	X.X	Y
	equivalent width (\AA)		
Range($\text{EW}_{\text{H}\alpha}$) ₁	H α equiv. width range	X.X	Y
	from Clump 1 (\AA)		
Range($\text{EW}_{\text{H}\alpha}$) ₂	H α equiv. width range	X.X	Y
	from Clump 2 (\AA)		

NOTE— * Given only $v \sin i$ and $2\pi R_*/P_{\text{rot}}$, $\cos i = 0.11^{+0.11}_{-0.08}$. Provenances are: 1: SED fit ⁴. 2: Gaia DR3 photometry and lack of lithium (see 3). 3: PARSEC v1.2S ²⁵. 4: Keck/HIRES. 5: TESS light curve. 6: Derived quantity. 7: Gaia DR3 geometric ²⁶.

in which the circumstellar material is made only of dust are also ruled out. While dust may be present, to explain the H α emission the clumps must include plasma with a significant population of hydrogen atoms in the $n=3$ excited state. While this plasma is undoubtedly sculpted by the star’s magnetic field, it could plausibly originate from three sites: the star, an old and undetected disk, or outgassing rocky bodies. This latter possibility would render CPVs as extrasolar analogs of the Jupiter-Io plasma torus (e.g. Ref. ³⁰).

The other potential analog for the CPVs are the σ Ori E variables, a rare subset of B stars with radiatively-driven winds that accumulate into warped plasma tori ^{7,24}. These tori tend to have dense antipodal accumulations of plasma sculpted by tilted-dipole magnetic fields, and the transits of these clumps are thought to produce the observed broadband photometric variability through bound-free scattering ⁷ and Thomson scattering ³¹. For σ Ori E and almost all of its analogs, the result is light curves that appear “simple”, resembling those of eclipsing binaries ²⁴. The two known exceptions, HD 37776 and HD 64740, show complex light curves resembling CPVs ^{4,32} and have spectropolarimetric magnetic field maps indicating strong contributions from higher-order magnetic moments ^{33,34}. There are two implications: first, the complexity of CPVs may be a direct consequence of magnetic fields with highly multipolar contributions. Second, CPVs could be a source of astrophysical false positives in photometric searches for eclipsing binaries and transiting exoplanets around young pre-main sequence M dwarfs ^{35,36}.

Pressing issues for future work include determining the composition and origin of the circumstellar material, understanding the exact role of the stellar magnetic field, and exploring the implied space weather experienced by the close-in rocky exoplanets that, statistically¹³, are likely to be present in most CPV systems.

The material's composition – either pure plasma, or else a dusty plasma – can be clarified by time-series optical and infrared spectrophotometry. While observations of CPVs in the optical have previously suggested chromaticity consistent with dust^{19,37,38}, a gray opacity source such as electron scattering in a plasma transiting over starspots might also produce chromatic features³⁹. The composition and size distribution of any dust that is present would be most easily resolved by measuring the extinction curve for one or more CPVs from 1-10 μm . Composition and size distributions similar to debris from rocky bodies seen around white dwarfs⁴⁰ would indicate a rocky-body origin. Compositions and sizes to the ISM would be indicative of condensed dust in an M dwarf wind, similar to that formed in the environments of more evolved stars⁴¹.

The role of the star's magnetic field could be better understood through new observations, and new theory. From the theoretical perspective, there is an urgent need for rigid-field (magneto)-hydrodynamic modeling to go beyond previous work^{7,24} and to explore the effects of non-dipolar field contributions. In particular, dynamo simulations of fully-convective M dwarfs have suggested that global-scale mean fields might be confined to a single hemisphere⁴²; such fields could yield accumulation surfaces quite different from those that have previously been explored²⁴. Observationally, spectropolarimetry has the potential to assess both the field strength and topology. An independent probe could also be connected to the recent work⁴³ showing that CPVs are variable radio emitters with emission components that can be both persistent, and also short-lived and highly polarized. In particular, detecting radio emission produced by an electron cyclotron maser instability would provide a measurement of the field strength at the site of the emitting region.

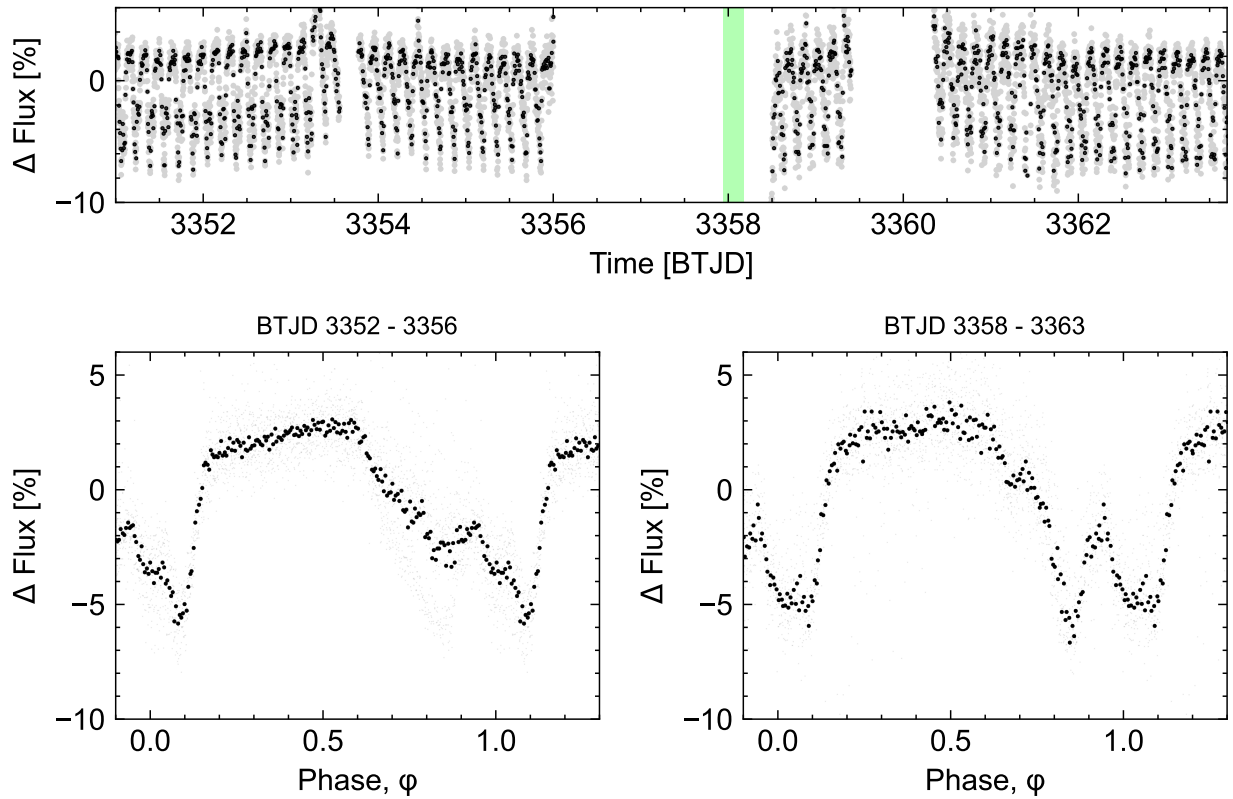
It is currently unclear what, if any, relationship CPVs have to the close-in exoplanets that exist around most M dwarfs¹³. However, 0.3-3% of young M dwarfs show the CPV phenomenon¹⁸, and our data show that the phenomenon occurs when clumps of circumstellar material transit the star. The implied geometric correction suggests that an appreciable minority (10-30%) of young M dwarfs – the rapidly rotating ones with centrifugal magnetospheres – host similar circumstellar environments to the CPVs.

Methods

Observations & Data Reduction

Photometry: TESS observed TIC 141146667 ($T=13.3$) in Sectors 14, 15, 21, 41, 48, and 75. Two-minute data were acquired during Sectors 41, 48 (TESS DDT039, PI: Kunimoto), and 75 (TESS Program G06030, PI: Bouma). The data from Sectors 14, 15, and 21 had a 30-minute cadence, which smears sharp features over the <4 hour period (see ¹⁹). The nearest known star, TIC 141146666 ($T=14.5$), is $25''$ from TIC 141146667 and is photometrically stable in the pixel-level TESS data.

Figure 1 shows the data from Sector 75, which were acquired using the camera that pointed closest to the ecliptic. The largest gap in coverage is from BTJD 3356.0 - 3358.5, and includes



Extended Data Figure 1: Photometric evolution of TIC 141146667 near the epoch of spectroscopic observation (green bar). **Panel a:** TESS simple aperture photometry. The main data gaps were caused by scattered light from the Earth (BTJD 3356-3358.5) and Moon (BTJD 3359.5-3360.5). **Panels b,c:** Folded light curve before and after spectroscopy. Although some evolution in the light curve morphology occurred between the two epochs, the large, complex eclipse feature remained present.

the Keck/HIRES observation epoch (green bar). There are no flux measurements reported during this interval because the Earth was within 25° the camera’s boresight, yielding high levels of scattered light. From BTJD 3359.4 - 3362.0, the Moon then passed within 25° of the camera’s boresight. Based on the observed level of scattered light in the optimal TIC 141146667 aperture, we manually masked out times from 3359.40 - 3360.13, and judged the remainder of the data during the lunar approach to be usable. The small data gaps from BTJD 3353.55 - 3353.77 and from BTJD 3360.12 - 3360.33 were caused by data downlinks at the spacecraft’s perigee and apogee, respectively.

Spectroscopy: We observed TIC 141146667 ($V=16.2$) with Keck/HIRES for five hours over a second-half night spanning UT 2024-02-17 10:47 to UT 2024-02-17 16:13. The star’s airmass over this window spanned $z=1.2$ - 2.2 , and we opted for a fixed 15 minute cadence over the entire sequence, except for a final 10 minute exposure due to increasing sky brightness at sunrise. We observed without the iodine cell and used the C2 decker ($0''.86 \times 14''.0$) in the red instrument configuration, yielding a spectral resolution $R \approx 45,0000$ ($\delta v \approx 6.7 \text{ km s}^{-1}$; $\delta v/v_{\text{eq}} \approx 0.05$). We binned the CCD readout by a factor of three in the spatial dimension, yielding $\approx 1,000$ photons ($S/N=33$) per pixel in the continuum at 6500 \AA , at minimum airmass. Strong winds contributed to $1''.2 \pm 0''.2$ seeing over the night, but conditions were otherwise favorable. We reduced the echelleogram to a one-dimensional spectrum using the standard techniques of the California Planet Survey⁴⁴. Figure 2b shows the result in the vicinity of $H\alpha$ without any additional processing.

Stellar Parameters

Radial Velocity—We measured radial velocities of TIC 141146667 from our HIRES spectra using a pipeline that we developed for rapidly rotating stars. Our method is based on template-matching against synthetic spectra produced by the PHOENIX stellar atmosphere code⁴⁵. We used the PHOENIX models with solar metallicity and alpha element abundances, and calibrated our pipeline using the standard stars described by⁴⁶. We used velocity standards spanning spectral types from G2 to M4 (Barnard’s Star), irrespective of rotation rate. We used `barycorrpy`⁴⁷ to calculate the velocity corrections due to Earth’s motion around the solar system barycenter and due to Earth’s daily rotation about its axis. Our analysis code reproduces the systemic velocities of known velocity standards⁴⁶ with an RMS of 0.66 km s^{-1} .

For TIC 141146667, we measured the radial velocities using regions near the K I (7700 \AA) resonance line and three TiO bandheads (5160 \AA , 5450 \AA , and 5600 \AA). We selected these regions because they provided the best matches between the synthetic and observed spectra. We then averaged the resulting redshift measurements over each order to produce the final measurement. We used the scatter of resulting velocity measurements between orders to assign the RV uncertainty at each epoch. The uncertainty-weighted mean systemic velocity over all epochs on 17 February 2024 was $\gamma = 0.6 \pm 1.5 \text{ km s}^{-1}$. The relative radial velocities about this mean are given in Table 2.

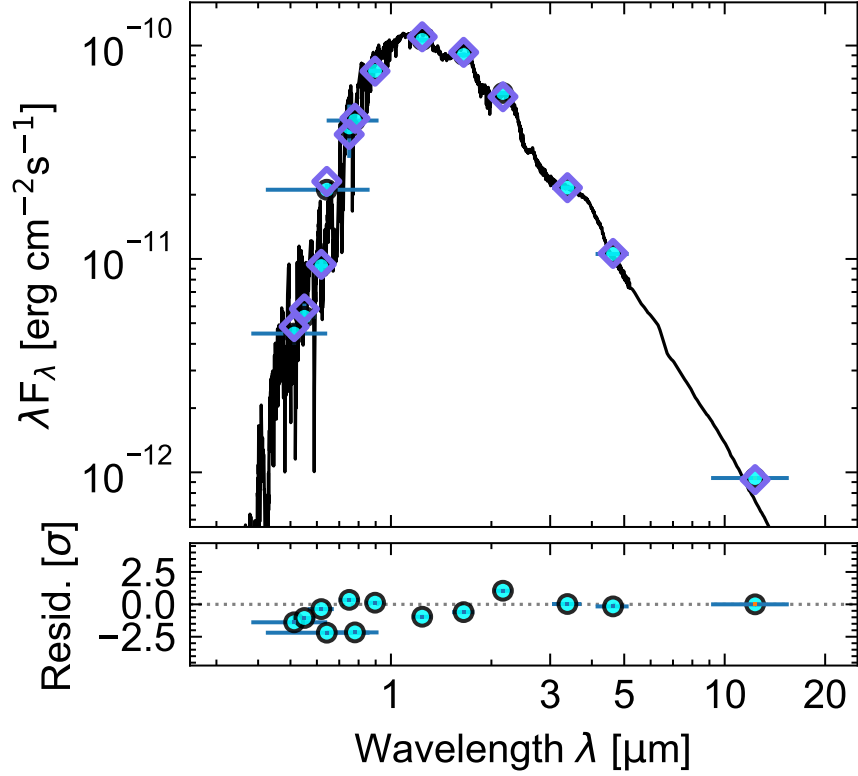
Viewing Orientation—We fitted the rotational broadening of the K I (7700 \AA) resonance line using the broadening kernel suggested by⁴⁸; taking the mean and standard deviation of the result-

ing value over all epochs yielded $v_{\text{eq}} \sin i = 138 \pm 8 \text{ km s}^{-1}$, consistent with the visual line broadening $\Delta\lambda \approx 3 \text{ \AA}$. The star’s equatorial velocity v_{eq} based on its apparent size and rotation period is $130 \pm 4 \text{ km s}^{-1}$. While this suggests that the viewing orientation could be nearly edge-on, the formal constraint is rather weak, with $i > 63^\circ$ at 2σ (2.5th percentile of the inclination posterior).

No Evidence For Binarity—Any significant periodicity in the radial velocity time-series is ruled out at the rotation period for semi-amplitudes above 2.85 km s^{-1} (at 3σ confidence). This sets an upper limit on the mass of any putative companion at the four hour period of $m \sin i < 2.4 M_{\text{Jup}}$. Regarding possible companions at wider separations, the Gaia DR3 renormalized unit weight error (RUWE), a proxy for the goodness of fit for a single-source astrometric model to the Gaia astrometry, is 1.23, within the usual range for apparently single sources. There are no resolved sources in the Gaia DR3 point source catalog. Finally, we checked the TESS light curve for evidence of secondary photometric periods by subtracting the mean CPV signal over each sector and performing a phase-dispersion minimization analysis^{49,50}. There were no secondary periods in the TESS data. Previous work⁴ has shown that about 30% of CPVs show evidence for excess noise above the Gaia single-source astrometric model, and about 40% of CPVs show evidence for unresolved binary companions based on the presence of secondary photometric periods. This agrees with analyses showing that multi-periodic low-mass stars are generally unresolved binaries⁵¹. Overall, the CPV binary fraction seems consistent with that for field M dwarfs⁵², pointing to a weak or non-existent connection between the CPV phenomenon and binarity. For TIC 141146667 specifically, while we find no evidence for stellar multiplicity, our data are minimally constraining for the scenario of a low-luminosity companion ($F_1/F_2 \lesssim 0.1$) at large orbital separations.

Effective temperature, radius, mass, and spectral type We adopted the star’s effective temperature and radius measured using the spectral energy distribution (SED) fitting procedure described by⁴. To summarize, this approach used `astroARIADNE`⁵⁴ with the BT-Settl stellar atmosphere models⁵³, assuming the⁵⁵ solar abundances and the⁵⁶ water line lists. This approach fitted for the stellar effective temperature, radius, reddening, surface gravity, metallicity, and distance by comparing the measured broadband magnitudes against pre-computed model grids. Specifically, we performed the fit using the broadband magnitudes from Gaia DR2, APASS, 2MASS, SDSS, and WISE $W1$ and $W2$. The resulting best-fit SED is shown in Figure 2. This method has the most constraining power for the star’s effective temperature ($2972 \pm 40 \text{ K}$) and radius ($0.42 \pm 0.02 R_\odot$); the surface gravity, metallicity, and reddening are typically only weakly constrained. We determined the star’s spectral type to be M5.5Ve by visually comparing the HIRES spectra against the photometric standards tabulated by⁵⁷, which agrees with the effective temperature from the SED fitting⁵⁸.

Given the effective temperature, stellar radius, and age range (35-150 Myr) derived below, we then estimated the stellar mass by interpolating against the PARSEC v1.2S isochrones²⁵. Specifically, we used the distance metric defined in Equation 8 of⁴ to select the model mass closest to a given observed temperature, radius, and age. This exercise yielded a mass of $M_\star = 0.20 \pm 0.01 M_\odot$ assuming an age of 35 Myr, or a mass of $0.25 \pm 0.01 M_\odot$ assuming an age of 150 Myr. These masses imply Keplerian corotation radii $R_{\text{cr}}/R_\star = 1.75 \pm 0.07$ and $R_{\text{cr}}/R_\star = 1.89 \pm 0.07$, respectively; this



Extended Data Figure 2: Spectral energy distribution of broadband photometric magnitudes plotted over the best-fit BT-Settl stellar atmosphere model⁵³. This plot was made from an adaptation of `astroARIADNE`⁵⁴. The photometry extends from the Gaia DR3 blue passband to WISE W3; the W4 passband (22 μm) did not yield a confident detection. This fit yields the star’s temperature and size. The lack of excess infrared flux relative to the photospheric model sets an upper limit on emission from circumstellar dust.

size scale is relevant because it is theoretically expected to set the inner boundary at which corotating material might accumulate (e.g.^{7,11}). Our final quoted M_\star and R_{cr} values adopt the average of these extremes and a quadrature sum of their statistical uncertainties; we caution however that a more precise age would be needed to resolve the systematic uncertainties in these parameters.

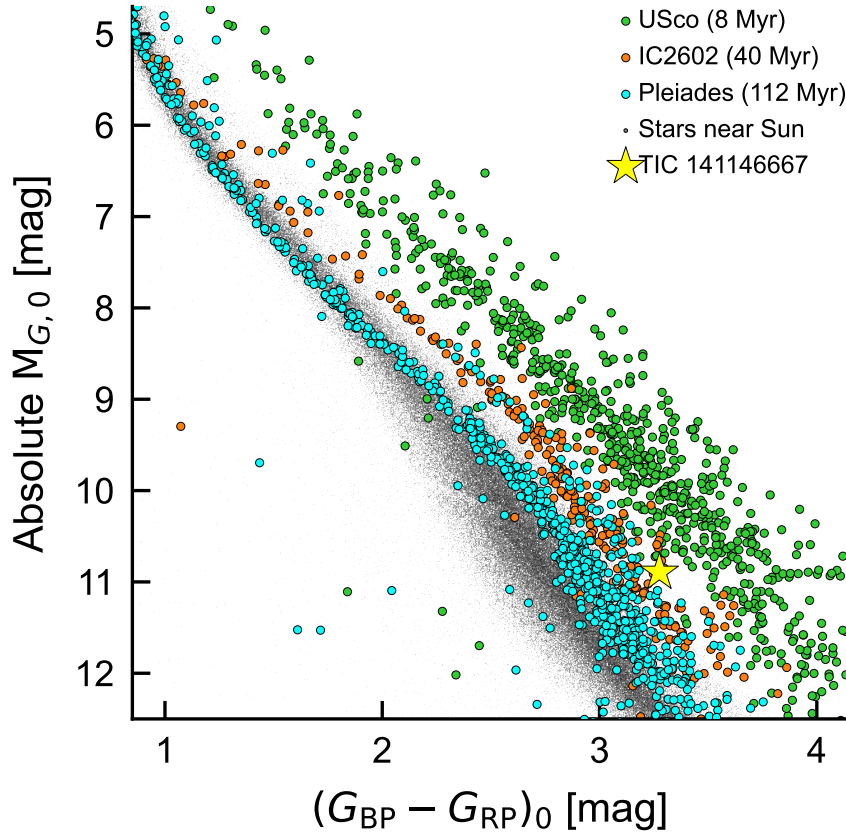
Age: No Obvious Association Membership—Previous work⁴ has found that over 90% of CPVs are associated with known young moving groups based on their positions and kinematics. TIC 141146667 is in the minority. We calculated the probability of TIC 141146667 being part of any of the nearby known groups using `BANYAN Σ` v1.2⁵⁹. That particular model classifies it as a field star at >99.9% confidence. We also searched the local vicinity of TIC 141146667 for neighbors with similar projected on-sky velocities using `comove`⁶⁰. This yielded no strong candidates for co-moving stars with projected tangential velocities $\Delta v_T < 5 \text{ km s}^{-1}$ that share its isochronal youth.

Age: Isochrones—The color and absolute magnitude of TIC 141146667 suggest that it is a pre-main sequence M dwarf, similar to all other known CPVs^{2,4,61}. The star’s proximity ($d=58$ pc) and its high galactic latitude ($b=+53^\circ$) yield negligible interstellar reddening along the line of sight⁶². Figure 3 shows the location of the star in the color–absolute magnitude diagram (CAMD) relative to young stellar populations including Upper Scorpius (USco), IC 2602, and the Pleiades. To make this diagram, we adopted the USco members in the δ Sco and σ Sco sub-associations from⁶³, and the IC 2602 and Pleiades members from⁶⁴. We assumed an average V -band extinction $A_V=\{0.12, 0.11, 0.10\}$ mag for USco⁶⁵, IC 2602⁶⁴, and the Pleiades⁶⁴ respectively. We dereddened the photometry using the extinction coefficients $k_X \equiv A_X/A_0$ tabulated in⁶⁶, assuming that $A_0 = 3.1E(B - V)$.

Figure 3 shows that TIC 141146667 falls between the USco and Pleiades sequences, while nearly overlapping with IC 2602. However, the precision of the implied age is set by the intrinsic scatter of these calibration sequences; the most luminous stars in the Pleiades of the same color have a similar absolute magnitude as TIC 141146667. Previous work⁶¹ has also noted that in the Gaia passbands, CPVs tend to be photometrically redder and more luminous than single stars in any given cluster, similar to other rapid rotators. While this effect complicates any attempt at age inference based on the Gaia photometry, it suggests that the Pleiades may be a better comparison population than IC 2602. Broadly, we take the star’s location in the color–absolute magnitude diagram to suggest age bounds $t_{\text{CAMD}} \sim 30\text{--}150$ Myr.

Age: Lithium—The depletion of lithium due to ${}^7\text{Li}(p, \alpha){}^4\text{He}$ burning in the cores of low-mass stars has been studied for over sixty years^{67–69}.⁷⁰ provided an instructive recent overview: an abbreviated summary is that cooler and younger M dwarfs can show the 6707.8 \AA doublet in absorption, $\gtrsim 10\%$ below their “continua”. Unlike Sun-like stars, the continuum for M dwarfs is poorly defined due to their molecular absorption. We attempted a lithium measurement by constructing a wavelength-binned and Doppler-corrected TIC 141146667 spectrum, assigning its uncertainties based on the measured scatter across the five hour dataset. We then compared this average spectrum against the nearest matching template from⁵⁷. The data show a small depression near the expected lithium wavelength, potentially consistent with a $\Delta\lambda \approx 3 \text{ \AA}$ line broadening. This feature nominally yields $\text{EW}_{\text{Li}} = 71_{13}^{+18} \text{ m\AA}$, where the statistical uncertainties are evaluated using a bootstrap resampling technique from the statistical uncertainties in the spectrum. The systematic uncertainties associated with the continuum normalization are larger, and likely comparable to the amplitude of the feature; we therefore treat the result of this measurement as a 2σ upper limit: $\text{EW}_{\text{Li}} < 107 \text{ m\AA}$.

Despite uncertainties in the details, what can be stated with confidence is that lithium is not abundant in the spectrum of TIC 141146667. Figure 4 compares our upper limit against the equivalent width measurements reported by⁷¹ based on the Gaia-ESO spectroscopic survey. If the star were $\lesssim 20$ Myr old, at its temperature we would expect to see lithium in abundance ($> 400 \text{ m\AA}$). Since we do not, we can set an empirical bound on the lithium-derived age of $t_{\text{Li,emp}} \gtrsim 20$ Myr. The⁷² lithium isochrones provide a point for theoretical comparison, and suggest that since $M_K = 6.67$ mag, $t_{\text{Li,th}} \gtrsim 35$ Myr is the theoretical age at which complete depletion occurs

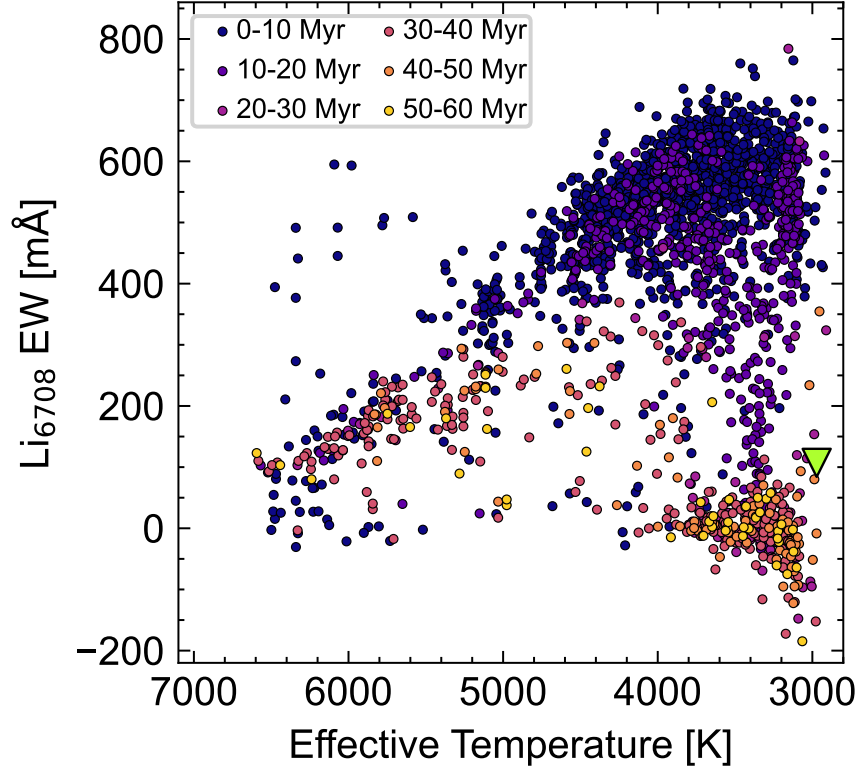


Extended Data Figure 3: Dereddened Gaia DR3 color vs. absolute magnitude diagram of TIC 141146667 and comparison samples. TIC 141146667 is on the pre-main sequence; stars with the same color on the main sequence are ≈ 1.5 magnitudes fainter. The star’s location in this diagram broadly suggests an age of 30-150 Myr.

in a star with this luminosity (see e.g. Figure 7 from ⁷⁰).

Age: Summary—The main indicators for the youth of TIC 141146667 are *i*) that it is a complex periodic variable, and *ii*) that it is 1.5 magnitudes brighter than main sequence stars of the same color, while showing no indicators for binarity. The first item constitutes evidence for youth since all known CPVs are $\lesssim 200$ Myr ⁴. The reference sequences for the Pleiades (112 Myr, ⁷³) show a few stars of equal luminosity and the same temperature, suggesting a photometric isochronal age upper limit $\lesssim 150$ Myr. The weak lithium absorption suggests an age of at least 20 Myr based on an empirical comparison using Gaia-ESO spectra, or at least 35 Myr based on the ⁷² isochrones. These considerations yield our adopted age range of 150 Myr.

Upper and Low Bounds on Dust—An upper limit on the amount of hot dust follows from the lack of an infrared excess. A lower limit follows if one assumes that most of the broadband optical depth comes from dust absorption and scattering, rather than any radiative processes associated



Extended Data Figure 4: An upper limit on photospheric lithium for TIC 141146667 (green triangle) yields a lower limit on the star’s age of $\gtrsim 20$ Myr. Comparison stars are from the Gaia-ESO survey ⁷¹; rich clusters in each age bin include NGC 2264 (4.5 Myr), λ Ori (8.7 Myr), γ^2 Vel (16.4 Myr), NGC 2547 (35.0 Myr), IC 2602 and IC 2391 (42.0 Myr), and NGC 2451A (50.0 Myr).

319 with the plasma.

320 How much dust is allowed, given the lack of an infrared excess? Figure 2 shows the SED.
 321 While AllWISE ⁷⁴ yielded a confident W3 detection (9.8σ), the W4 extraction yielded only a
 322 marginal (1.7σ) indication of detectable flux. Similar to other CPVs ^{2,4}, the photometric uncer-
 323 tainties from WISE W1 and W2 allow at most a $\lesssim 2\%$ excess at $3-5\ \mu\text{m}$ relative to the stellar
 324 photosphere, and a $\lesssim 5\%$ excess at $10\ \mu\text{m}$ (W3). To estimate the implied mass bound, we assume
 325 $T_{\text{dust}}=1500\ \text{K}$, typical for dust near the star (see ¹⁷ for discussion regarding dust sublimation). We
 326 then treat emission from the dust and the star as Planck functions, requiring $F_{\lambda,\star} > f \cdot F_{\lambda,\text{dust}}$,
 327 for f the scaling factor set by the WISE photometric uncertainty. For this condition to hold, we
 328 find that the bolometric flux ratio $F_{\text{dust}}/F_{\star} < 6 \cdot 10^{-3}$. Scaling the associated luminosities ($L =$
 329 $\sigma_{\text{SB}} T_{\text{eff}}^4 / (4\pi R^2)$) implies an emitting area for the dust $< 10\%$ of the star’s surface area. Converting
 330 this constraint to a dust mass requires an assumption regarding the grain properties; assuming a
 331 grain density $\rho_{\text{d}}=3\ \text{g cm}^{-3}$ typical for silicate grains, and a fixed grain size $a=1\ \mu\text{m}$ ^{19,37,38} yields
 332 an upper limit of $M_{\text{dust}} \lesssim 10^{17}\ \text{g}$.

By way of comparison, the lower limit follows from requiring the optical depth τ to be at least unity. The optical depth can be written $\tau = n\sigma\ell = N\sigma$, where σ is the cross-section, n is the number density, ℓ is the path length, and N is the column density. For spherical dust grains in the optical, $\sigma = Q_{\text{ext}}\pi a^2$, where Q_{ext} is the extinction efficiency parameter, tabulated e.g. by ⁷⁵ in their Figure 13. ⁷⁶ calculated the relevant cloud mass scaling assuming a spherical dust clump of size r , and they found

$$M_{\text{dust}} \gtrsim 1.6 \cdot 10^{15} \text{ g} \left(\frac{\tau}{1}\right) \left(\frac{Q_{\text{ext}}}{3}\right)^{-1} \left(\frac{r}{0.1 R_{\star}} \frac{R_{\star}}{0.34 R_{\odot}}\right)^2 \left(\frac{a}{1 \mu\text{m}}\right) \left(\frac{\rho_{\text{d}}}{3 \text{ g cm}^{-3}}\right). \quad (1)$$

By way of comparison, prominences of the Sun typically have gas masses of order 10^{14} g - 10^{16} g ²⁹, whereas a planetesimal of this mass with a bulk density of 1 g cm^{-3} would have a diameter of order one kilometer. Halley's comet has a mass of order 10^{17} g ⁷⁷, of which of order one part in a thousand is shed per orbit, most of which inspirals toward the Sun due to Poynting-Robertson drag.

Broadly, these calculations suggest that if dust is responsible for the broadband variability of CPVs, it would need to be concentrated in clumps with masses in the range of 10^{15} - 10^{17} g .

Spectroscopic Variability

The full HIRES coverage spans 3650-7960 Å, and variable emission is visible in Balmer lines from $n=10 \rightarrow 2$, Ca[H] and Ca[K], the Mg[I] b triplet, and the 5875 He[I] emission line.

Spectral Behavior of Other Lines First, chromospheric:

Hγ, Hδ Line ratios.

Ca [K] Also shows some high-velocity emission. So, the emitting material has calcium ions.

He 5880 Also variable...

Magnesium b orders Shows some variability that is horrendously blended.

K[I] 7700 Literally the only obvious photospheric line.

Modeling the Emitting Clump The density and mass of the material...

1. Rebull, L. M. *et al.* Rotation in the Pleiades with K2. II. Multiperiod Stars. *Astron. J.* **152**, 114 (2016).
2. Stauffer, J. *et al.* Orbiting Clouds of Material at the Keplerian Co-rotation Radius of Rapidly Rotating Low-mass WTTs in Upper Sco. *Astron. J.* **153**, 152 (2017).
3. Rebull, L. M. *et al.* Rotation of Low-mass Stars in Upper Scorpius and ρ Ophiuchus with K2. *Astron. J.* **155**, 196 (2018).

Parameter	Host	Source
Identifiers		
TIC	141146667	TESS
Gaia	860453786736413568	Gaia DR3
Astrometry & Radial Velocity		
α_{2000}	11:05:15.09	Gaia DR3
δ_{2000}	+59 15 05.57	Gaia DR3
μ_{α} (mas yr ⁻¹)	-73.933 ± 0.022	Gaia DR3
μ_{δ} (mas yr ⁻¹)	32.262 ± 0.024	Gaia DR3
π (mas)	17.324 ± 0.025	Gaia DR3
RUWE	1.23	Gaia DR3
RV (km s ⁻¹)	0.61 ± 1.47	HIRES
Photometry		
<i>TESS</i> (mag)	13.283 ± 0.010	TIC8
<i>G</i> (mag)	14.701 ± 0.002	Gaia DR3
<i>G</i> _{BP} (mag)	16.664 ± 0.008	Gaia DR3
<i>G</i> _{RP} (mag)	13.398 ± 0.006	Gaia DR3
<i>G</i> _{BP} - <i>G</i> _{RP} (mag)	3.276 ± 0.010	Gaia DR3
<i>J</i> (mag)	11.401 ± 0.022	2MASS
<i>H</i> (mag)	10.793 ± 0.021	2MASS
<i>K_s</i> (mag)	10.473 ± 0.016	2MASS
<i>W1</i> (mag)	10.276 ± 0.023	ALLWISE
<i>W2</i> (mag)	10.070 ± 0.020	ALLWISE
<i>W3</i> (mag)	9.838 ± 0.045	ALLWISE
Physical Properties		
<i>T_{eff}</i> (K)	2972 ± 40	⁴ SED fit
<i>R</i> _★ (<i>R</i> _☉)	0.42 ± 0.02	⁴ SED fit
<i>P</i> _{rot} (hours)	3.930 ± 0.001	TESS
<i>v</i> _{eq} (km s ⁻¹)	130±4	Derived
<i>v</i> _{eq} sin <i>i</i> _★ (km s ⁻¹)	138 ± 8	HIRES
<i>i</i> _★ (°)	>63	Derived
<i>A_V</i> (mag)	0	⁶²
<i>M</i> _★ (<i>M</i> _☉)	0.22 ± 0.02	PARSEC ²⁵
EW _{Li} (mÅ)	<107	HIRES (2σ)
<i>t</i> _{CAMD} (Myr)	30-150	Gaia DR3
<i>t</i> _{Li,emp} (Myr)	>20	HIRES, ⁷¹
<i>t</i> _{Li,th} (Myr)	>35	HIRES, ⁷²
<i>t</i> _{adopted} (Myr)	35-150	—

Extended Data Table 1: Properties of TIC 141146667. References: Gaia DR3 ²⁶, TESS ²², TIC8 ⁷⁸, 2MASS ⁷⁹, ALLWISE ⁷⁴.

Time [JD _{UTC}]	RV (km s ⁻¹)	σ_{RV} (km s ⁻¹)
60357.450329	2.73	5.86
60357.461255	-4.40	2.37
60357.472181	-0.19	2.64
60357.483109	3.84	2.87
60357.494030	7.53	7.53
60357.504949	-1.98	1.44
60357.515873	1.02	1.21
60357.526794	0.64	7.03
60357.537717	-2.91	2.71
60357.548639	8.93	6.75
60357.559566	5.95	8.84
60357.570487	-2.25	3.06
60357.581408	1.84	1.34
60357.592330	2.41	8.24
60357.603251	-7.04	3.94
60357.614172	-2.24	3.07
60357.625095	-2.83	7.55
60357.636019	-0.59	2.26
60357.646940	1.84	2.91
60357.657861	4.54	3.95
60357.668781	6.21	12.14

Extended Data Table 2: TIC 141146667 radial velocities relative to the systemic velocity.

4. Bouma, L. G. *et al.* Transient Corotating Clumps around Adolescent Low-mass Stars from Four Years of TESS. *Astron. J.* **167**, 38 (2024).
5. Koen, C. Starspot modelling of the TESS light curve of CVSO 30. *Astron. Astrophys.* **647**, L1 (2021).
6. Collier Cameron, A. & Robinson, R. D. Fast H-alpha variations on a rapidly rotating cool main sequence star- I. Circumstellar clouds. *Mon. Not. R. Astron. Soc.* **236**, 57–87 (1989).
7. Townsend, R. H. D. & Owocki, S. P. A rigidly rotating magnetosphere model for circumstellar emission from magnetic OB stars. *Mon. Not. R. Astron. Soc.* **357**, 251–264 (2005).
8. Dunstone, N. J., Collier Cameron, A., Barnes, J. R. & Jardine, M. The coronal structure of Speedy Mic - II. Prominence masses and off-disc emission. *Mon. Not. R. Astron. Soc.* **373**, 1308–1320 (2006).
9. Petit, V. *et al.* A magnetic confinement versus rotation classification of massive-star magnetospheres. *Mon. Not. R. Astron. Soc.* **429**, 398–422 (2013).
10. Waugh, R. F. P. & Jardine, M. M. Magnetic confinement of dense plasma inside (and outside) stellar coronae. *Mon. Not. R. Astron. Soc.* **514**, 5465–5477 (2022).
11. Daley-Yates, S. & Jardine, M. M. Simulating stellar coronal rain and slingshot prominences. *Mon. Not. R. Astron. Soc.* **534**, 621–633 (2024).
12. National Academies of Sciences, E. & Medicine. *Pathways to Discovery in Astronomy and Astrophysics for the 2020s* (The National Academies Press, Washington, DC, 2023). URL <https://nap.nationalacademies.org/catalog/26141/pathways-to-discovery-in-astronomy-and-astrophysics-for-the-2020s>.
13. Dressing, C. D. & Charbonneau, D. The Occurrence of Potentially Habitable Planets Orbiting M Dwarfs Estimated from the Full Kepler Dataset and an Empirical Measurement of the Detection Sensitivity. *Astrophys. J.* **807**, 45 (2015).
14. Ribas, Á., Bouy, H. & Merín, B. Protoplanetary disk lifetimes vs. stellar mass and possible implications for giant planet populations. *Astron. Astrophys.* **576**, A52 (2015).
15. France, K. *et al.* The Ultraviolet Radiation Environment around M dwarf Exoplanet Host Stars. *Astrophys. J.* **763**, 149 (2013).
16. Günther, M. N. *et al.* Stellar Flares from the First TESS Data Release: Exploring a New Sample of M Dwarfs. *Astron. J.* **159**, 60 (2020).
17. Zhan, Z. *et al.* Complex Rotational Modulation of Rapidly Rotating M Stars Observed with TESS. *Astrophys. J.* **876**, 127 (2019).
18. Rebull, L. M. *et al.* Rotation of Low-mass Stars in Taurus with K2. *Astron. J.* **159**, 273 (2020).

- 396 19. Günther, M. N. *et al.* Complex Modulation of Rapidly Rotating Young M Dwarfs: Adding
397 Pieces to the Puzzle. *Astron. J.* **163**, 144 (2022).
- 398 20. Donati, J. F. *et al.* Surface differential rotation and prominences of the Lupus post T Tauri star
399 RX J1508.6-4423. *Mon. Not. R. Astron. Soc.* **316**, 699–715 (2000).
- 400 21. Skelly, M. B. *et al.* Doppler images and chromospheric variability of TWA 6. *Mon. Not. R.*
401 *Astron. Soc.* **385**, 708–718 (2008).
- 402 22. Ricker, G. R. *et al.* Transiting Exoplanet Survey Satellite (TESS). *Journal of Astronomical*
403 *Telescopes, Instruments, and Systems* **1**, 014003 (2015).
- 404 23. Vogt, S. S. *et al.* *SPIE Conference Series*, vol. 2198 (1994).
- 405 24. Townsend, R. H. D. Exploring the photometric signatures of magnetospheres around helium-
406 strong stars. *Mon. Not. R. Astron. Soc.* **389**, 559–566 (2008).
- 407 25. Chen, Y. *et al.* Improving PARSEC models for very low mass stars. *Mon. Not. R. Astron.*
408 *Soc.* **444**, 2525–2543 (2014).
- 409 26. Gaia Collaboration *et al.* Gaia Data Release 3. Summary of the content and survey properties.
410 *Astron. Astrophys.* **674**, A1 (2023).
- 411 27. Collier Cameron, A. & Woods, J. A. Prominence activity in G dwarfs of the alpha Persei
412 cluster. *Mon. Not. R. Astron. Soc.* **258**, 360–370 (1992).
- 413 28. Cang, T. Q. *et al.* Magnetic field and prominences of the young, solar-like, ultra-rapid rotator
414 V530 Persei. *Astron. Astrophys.* **643**, A39 (2020).
- 415 29. Vial, J.-C. & Engvold, O. *Solar Prominences*, vol. 415 of *Astrophysics and Space Science*
416 *Library* (2015).
- 417 30. Bagenal, F. & Sullivan, J. D. Direct plasma measurements in the Io torus and inner magneto-
418 sphere of Jupiter. *J. Geophys. Res.* **86**, 8447–8466 (1981).
- 419 31. Berry, I. D., Owocki, S. P., Shultz, M. E. & ud-Doula, A. Electron scattering emission in
420 the light curves of stars with centrifugal magnetospheres. *Mon. Not. R. Astron. Soc.* **511**,
421 4815–4825 (2022).
- 422 32. Mikulášek, Z. *et al.* What’s New with Landstreet’s Star HD 37776 (V901 Ori)? In Wade, G.,
423 Alecian, E., Bohlender, D. & Sigut, A. (eds.) *Stellar Magnetism: A Workshop in Honour of*
424 *the Career and Contributions of John D. Landstreet*, vol. 11, 46–53 (2020). 1912.04121.
- 425 33. Kochukhov, O., Lundin, A., Romanyuk, I. & Kudryavtsev, D. The Extraordinary Complex
426 Magnetic Field of the Helium-strong Star HD 37776. *Astrophys. J.* **726**, 24 (2011).
- 427 34. Shultz, M. E. *et al.* The magnetic early B-type stars I: magnetometry and rotation. *Mon. Not.*
428 *R. Astron. Soc.* **475**, 5144–5178 (2018).

- 429 35. Johns-Krull, C. M. *et al.* H α Variability in PTFO8-8695 and the Possible Direct Detection of
430 Emission from a 2 Million Year Old Evaporating Hot Jupiter. *Astrophys. J.* **830**, 15 (2016).
- 431 36. Bouma, L. G. *et al.* PTFO 8-8695: Two Stars, Two Signals, No Planet. *Astron. J.* **160**, 86
432 (2020).
- 433 37. Tanimoto, Y. *et al.* Evidence for planetary hypothesis for PTFO 8-8695 b with five-year
434 optical/infrared monitoring observations. *PASJ* **72**, 23 (2020).
- 435 38. Koen, C. Multifilter observations of the complex periodic variations in eight pre-main se-
436 quence stars. *Mon. Not. R. Astron. Soc.* **518**, 2921–2937 (2023).
- 437 39. Rackham, B. V., Apai, D. & Giampapa, M. S. The Transit Light Source Effect: False Spec-
438 tral Features and Incorrect Densities for M-dwarf Transiting Planets. *Astrophys. J.* **853**, 122
439 (2018).
- 440 40. Reach, W. T., Lisse, C., von Hippel, T. & Mullally, F. The Dust Cloud around the White Dwarf
441 G 29-38. II. Spectrum from 5 to 40 μ m and Mid-Infrared Photometric Variability. *Astrophys.*
442 *J.* **693**, 697–712 (2009).
- 443 41. Marigo, P. *et al.* Evolution of asymptotic giant branch stars. II. Optical to far-infrared
444 isochrones with improved TP-AGB models. *Astron. Astrophys.* **482**, 883–905 (2008).
- 445 42. Brown, B. P., Oishi, J. S., Vasil, G. M., Lecoanet, D. & Burns, K. J. Single-hemisphere
446 Dynamos in M-dwarf Stars. *Astrophys. J.* **902**, L3 (2020).
- 447 43. Kaur, S. *et al.* Hints of auroral and magnetospheric polarized radio emission from the scallop-
448 shell star 2MASS J05082729–2101444. *Astron. Astrophys.* **691**, L17 (2024).
- 449 44. Howard, A. W. *et al.* The California Planet Survey. I. Four New Giant Exoplanets. *Astrophys.*
450 *J.* **721**, 1467–1481 (2010).
- 451 45. Husser, T. O. *et al.* A new extensive library of PHOENIX stellar atmospheres and synthetic
452 spectra. *Astron. Astrophys.* **553**, A6 (2013).
- 453 46. Chubak, C. *et al.* Precise Radial Velocities of 2046 Nearby FGKM Stars and 131 Standards.
454 *arXiv e-prints* arXiv:1207.6212 (2012).
- 455 47. Kanodia, S. & Wright, J. Python Leap Second Management and Implementation of Precise
456 Barycentric Correction (barycorrpy). *Research Notes of the American Astronomical Society* **2**,
457 4 (2018).
- 458 48. Gray, D. F. *The Observation and Analysis of Stellar Photospheres* (2008).
- 459 49. Stellingwerf, R. F. Period determination using phase dispersion minimization. *Astrophys. J.*
460 **224**, 953–960 (1978).
- 461 50. Bhatti, W. *et al.* waqasbhatti/astrobases: astrobases v0.5.3. Zenodo (2021).

51. Tokovinin, A. & Briceño, C. Yes, Multi-periodic Dwarfs in Upper Scorpius Are Binaries. *Astron. J.* **156**, 138 (2018).
52. Winters, J. G. *et al.* The Solar Neighborhood. XLV. The Stellar Multiplicity Rate of M Dwarfs Within 25 pc. *Astron. J.* **157**, 216 (2019).
53. Allard, F., Homeier, D. & Freytag, B. Models of very-low-mass stars, brown dwarfs and exoplanets. *Philosophical Transactions of the Royal Society A: Mathematical, Physical and Engineering Sciences* **370**, 2765–2777 (2012).
54. Vines, J. I. & Jenkins, J. S. ARIADNE: measuring accurate and precise stellar parameters through SED fitting. *Mon. Not. R. Astron. Soc.* **513**, 2719–2731 (2022).
55. Asplund, M., Grevesse, N., Sauval, A. J. & Scott, P. The Chemical Composition of the Sun. *ARA&A* **47**, 481–522 (2009).
56. Barber, R. J., Tennyson, J., Harris, G. J. & Tolchenov, R. N. A high-accuracy computed water line list. *Mon. Not. R. Astron. Soc.* **368**, 1087–1094 (2006).
57. Bochanski, J. J., West, A. A., Hawley, S. L. & Covey, K. R. Low-Mass Dwarf Template Spectra from the Sloan Digital Sky Survey. *Astron. J.* **133**, 531–544 (2007).
58. Pecaú, M. J. & Mamajek, E. E. Intrinsic Colors, Temperatures, and Bolometric Corrections of Pre-main-sequence Stars. *Astrophys. J. Suppl.* **208**, 9 (2013).
59. Gagné, J. *et al.* BANYAN. XI. The BANYAN Σ Multivariate Bayesian Algorithm to Identify Members of Young Associations with 150 pc. *Astrophys. J.* **856**, 23 (2018).
60. Tofflemire, B. M. *et al.* TESS Hunt for Young and Maturing Exoplanets (THYME). V. A Sub-Neptune Transiting a Young Star in a Newly Discovered 250 Myr Association. *Astron. J.* **161**, 171 (2021).
61. Stauffer, J. *et al.* Even More Rapidly Rotating Pre-main-sequence M Dwarfs with Highly Structured Light Curves: An Initial Survey in the Lower Centaurus-Crux and Upper Centaurus-Lupus Associations. *Astron. J.* **161**, 60 (2021).
62. Green, G. M., Schlafly, E., Zucker, C., Speagle, J. S. & Finkbeiner, D. A 3D Dust Map Based on Gaia, Pan-STARRS 1, and 2MASS. *Astrophys. J.* **887**, 93 (2019).
63. Ratzenböck, S. *et al.* Significance mode analysis (SigMA) for hierarchical structures. An application to the Sco-Cen OB association. *Astron. Astrophys.* **677**, A59 (2023).
64. Hunt, E. L. & Reffert, S. Improving the open cluster census. III. Using cluster masses, radii, and dynamics to create a cleaned open cluster catalogue. *Astron. Astrophys.* **686**, A42 (2024).
65. Pecaú, M. J. & Mamajek, E. E. The star formation history and accretion-disc fraction among the K-type members of the Scorpius-Centaurus OB association. *Mon. Not. R. Astron. Soc.* **461**, 794–815 (2016).

66. Gaia Collaboration *et al.* Gaia Data Release 2. Summary of the contents and survey properties. *Astron. Astrophys.* **616**, A1 (2018).
67. Hayashi, C. & Nakano, T. Evolution of Stars of Small Masses in the Pre-Main-Sequence Stages. *Progress of Theoretical Physics* **30**, 460–474 (1963).
68. Bildsten, L., Brown, E. F., Matzner, C. D. & Ushomirsky, G. Lithium Depletion in Fully Convective Pre-Main-Sequence Stars. *Astrophys. J.* **482**, 442–447 (1997).
69. Burke, C. J., Pinsonneault, M. H. & Sills, A. Theoretical Examination of the Lithium Depletion Boundary. *Astrophys. J.* **604**, 272–283 (2004).
70. Wood, M. L. *et al.* TESS Hunt for Young and Maturing Exoplanets (THYME). IX. A 27 Myr Extended Population of Lower Centaurus Crux with a Transiting Two-planet System. *Astron. J.* **165**, 85 (2023).
71. Jeffries, R. D. *et al.* The Gaia-ESO Survey: empirical estimates of stellar ages from lithium equivalent widths (EAGLES). *Mon. Not. R. Astron. Soc.* **523**, 802–824 (2023).
72. Feiden, G. A. Magnetic inhibition of convection and the fundamental properties of low-mass stars. III. A consistent 10 Myr age for the Upper Scorpius OB association. *Astron. Astrophys.* **593**, A99 (2016).
73. Dahm, S. E. Reexamining the Lithium Depletion Boundary in the Pleiades and the Inferred Age of the Cluster. *Astrophys. J.* **813**, 108 (2015). URL <https://ui.adsabs.harvard.edu/abs/2015ApJ...813..108D>.
74. Cutri, R. M. *et al.* VizieR Online Data Catalog: AllWISE Data Release (Cutri+ 2013). *VizieR Online Data Catalog* II/328 (2021).
75. Croll, B. *et al.* Multiwavelength Observations of the Candidate Disintegrating Sub-Mercury KIC 12557548b. *Astrophys. J.* **786**, 100 (2014).
76. Sanderson, H., Jardine, M., Collier Cameron, A., Morin, J. & Donati, J. F. Can scallop-shell stars trap dust in their magnetic fields? *Mon. Not. R. Astron. Soc.* **518**, 4734–4745 (2023).
77. Rickman, H. The nucleus of comet Halley: Surface structure, mean density, gas and dust production. *Advances in Space Research* **9**, 59–71 (1989).
78. Stassun, K. G. *et al.* The Revised TESS Input Catalog and Candidate Target List. *Astron. J.* **158**, 138 (2019).
79. Skrutskie, M. F. *et al.* The Two Micron All Sky Survey (2MASS). *Astron. J.* **131**, 1163–1183 (2006).

Acknowledgments The author thanks X, Y, Z. L.G.B. was supported by... Acknowledge TESS... Acknowledge use of IRSA.

529 **Author Contributions** ...

530 **Data Availability** ...

531 **Competing Interests** The authors declare that they have no competing financial interests.

532 **Correspondence** Correspondence and requests for materials should be addressed to ...

533 **Code availability** We provide access to a GitHub repository including all code created for the analysis of
534 this project that is not already publicly available.